Supporting Information

Elucidating the Oxygen Storage-Release Dynamics in Ceria Nanorods by Combined Multi-Wavelength Raman Spectroscopy and DFT

Marc Ziemba[1], M. Verónica Ganduglia-Pirovano[2], Christian Hess[1*]

[1]Eduard-Zintl-Institute of Inorganic and Physical Chemistry, Technical University of Darmstadt, Alarich-Weiss-Str. 8, 64287 Darmstadt, Germany

*email: christian.hess@tu-darmstadt.de

[2]Instituto de Catálisis y Petroleoquímica - Consejo Superior de Investigaciones Científicas, Marie Curie 2, 28049 Madrid, Spain

Experimental Section

Catalyst Preparation. The synthesis of the ceria nanorods was realized by a hydrothermal synthesis based on previous studies.[1] Briefly, 79 ml of a 9 M NaOH solution (Grüssing GmbH, 98%) is prepared first. In another beaker the precursor $CeCl_3 \cdot 7H_2O$ (Alfa Aesar, 99%) is dissolved into 11 ml of deionized water (electrical conductivity <3 μSm^{-1}). This solution is added to the NaOH solution, stirred for 30 min, and then placed in a PTFE (Polytetrafluoroethylene) autoclave with a volume of about 140 mL. In addition, the autoclave is heated from approximately 25 °C to 140 °C for 48 h with a heating rate of 1 °C/min. After cooling to room temperature, the resulting CeO_2 is centrifuged off and washed three times with deionized water, before it is dried for at least 24 h at 85 °C in an oven. The synthesis of the ceria nanocubes is, with a few exceptions, analogous to that of the nanorods and is also based on previous studies.[2] In contrast to the rods, $Ce(NO_3)_3 \cdot 6H_2O$ (Alfa Aesar, 99.5%) is used as precursor, which was dissolved into 11 ml of deionized water. After that the solution is added to a 79 mL 6 M NaOH solution, which was placed in the PTFE (Polytetrafluoroethylene) autoclave: After that, the autoclave is heated from approximately 25 °C to 180 °C for 18 h with a heating rate of 1 °C/min. After cooling to room temperature, the resulting CeO_2 is centrifuged off and washed three times with deionized water, before it is dried for at least 24 h at 85 °C in an oven.

Transmission Electron Microscopy. The transmission electron microscope (JEOL JEM-2100F, Tokyo, Japan) is equipped with a Schottky field emitter and operates at a nominal acceleration voltage of 200 kV. For preparation, the sample was dispersed in an ultrasonic bath for 30 s in ethanol and then placed on a carbon grid (Plano). After drying, the grid was coated with carbon (Bal-Tec MED010), so that charging by the electron beam is prevented.

For additional structural analysis, an FFT of Figure 1A was calculated of each area, in which the white arrows indicate the distance of the lattice planes. After that a height profile of the diffraction pattern was created to make the patterns more visible. Then the patterns of the FFT in Figure S3A were masked with the help of Figure S3B and an inverse FFT was created. This is shown schematically in Figure S3 for the CeO_2(100) area. The same procedure was also used for the CeO_2(110) region, but only the inverse FFT is shown here (see Figure S4).

BET. N_2 adsorption at 77 K was conducted on a SURFER (Thermo Fisher Scientific). Prior the measurement, the sample was outgassed at 80 °C in high vacuum (10^{-6} bar) for 48 h. To determine the specific surface area the N_2 adsorption curve was fitted to the BET model.[3]

XRD. Powder X-ray diffraction patterns were recorded on a Stoe Stadi P diffractometer with Ge(111)-Monochromator, $Cu_{K\alpha}$ radiation (λ=1.54060 Å) and a MYTHEN-1K Dectris detector, using a flat sample holder in transmission geometry.

***In situ* Raman Spectroscopy (385 nm).** *In situ* Raman spectra with an excitation wavelength of 385 nm were recorded on a Raman spectrometer described previously[4,5] using a commercial CCR1000 cell

(Linkam Scientific Instruments) with a sapphire window. The power of the laser at the sample was 5.1 mW. Before the measurements the ceria rods were heated for 1 h at 120 °C at a flow rate of 50 mL min^{-1} (25% O_2 in He). Spectra were obtained from an average of two spectra with a measuring time of 30 min each. The sample was then cooled to 25 °C before another spectrum was recorded analogously. Spectra presented in this work were first normalized to the most intense band and, after that, the background was removed.

***In situ* Raman Spectroscopy (532 nm).** Raman spectra were recorded on a HL5R transmission spectrometer (Kaiser Optical) employing a frequency-doubled Nd:YAG laser (Cobolt) for excitation at 532 nm, as described previously.[6,7] The spectral resolution is specified as 5 cm^{-1}, and the stability of the band positions is better than 0.3 cm^{-1}. The laser power at the position of the sample was 1 mW. For the *in situ* measurements 20-25 mg of the sample was placed in a stainless-steel sample holder (diameter: 8 mm; depth: 0.5 mm) using a gas flow of 25 % O_2 in Ar (total flow rate: 100 mL/min). Rods were measured using an exposure time of 100 s and 3 accumulations and cubes with an exposure time of 40 s and 5 accumulations. For each measurement an auto new dark and a cosmic ray filter was used. As a result, the total measuring time amounted to about 1200 s for rods and 800 s for cubes. Hence, for each experimental condition (gas phase, temperature), two Raman spectra were recorded for the rods and three for the cubes. Thus, the residence time of the sample is approximately the same under any conditions. All spectra were normalized to the most intense band, i.e., the F_{2g} band. F_{2g} positions were determined by curve fitting using Lorentzian functions.

***In situ* Raman Spectroscopy (633 nm).** For the Raman spectra with 633 nm excitation a diode laser (Ondax) is used in combination with a HoloSpec f/1.8i transmission spectrometer (Kaiser Optical) and a commercial CCR1000 cell (Linkam Scientific Instruments) with quartz window. The spectral resolution of the spectrometer is specified as 5 cm^{-1}, and the stability of the band positions is better than 0.5 cm^{-1}. The power of the laser at the sample position was 2 mW. Measurements were performed using an exposure time of 90 s and 5 accumulations. For each measurement an auto new dark and a cosmic ray filter was used. As a result, the total measuring time amounted to about 1800 s. Prior to the measurement the ceria rods were heated for 2 h at 120 °C at a flow rate of 50 mL min^{-1} (25% O_2 in N_2); then the spectrum was recorded at 25 °C under the same gas phase. Spectra presented in this work were normalized to the F_{2g} band.

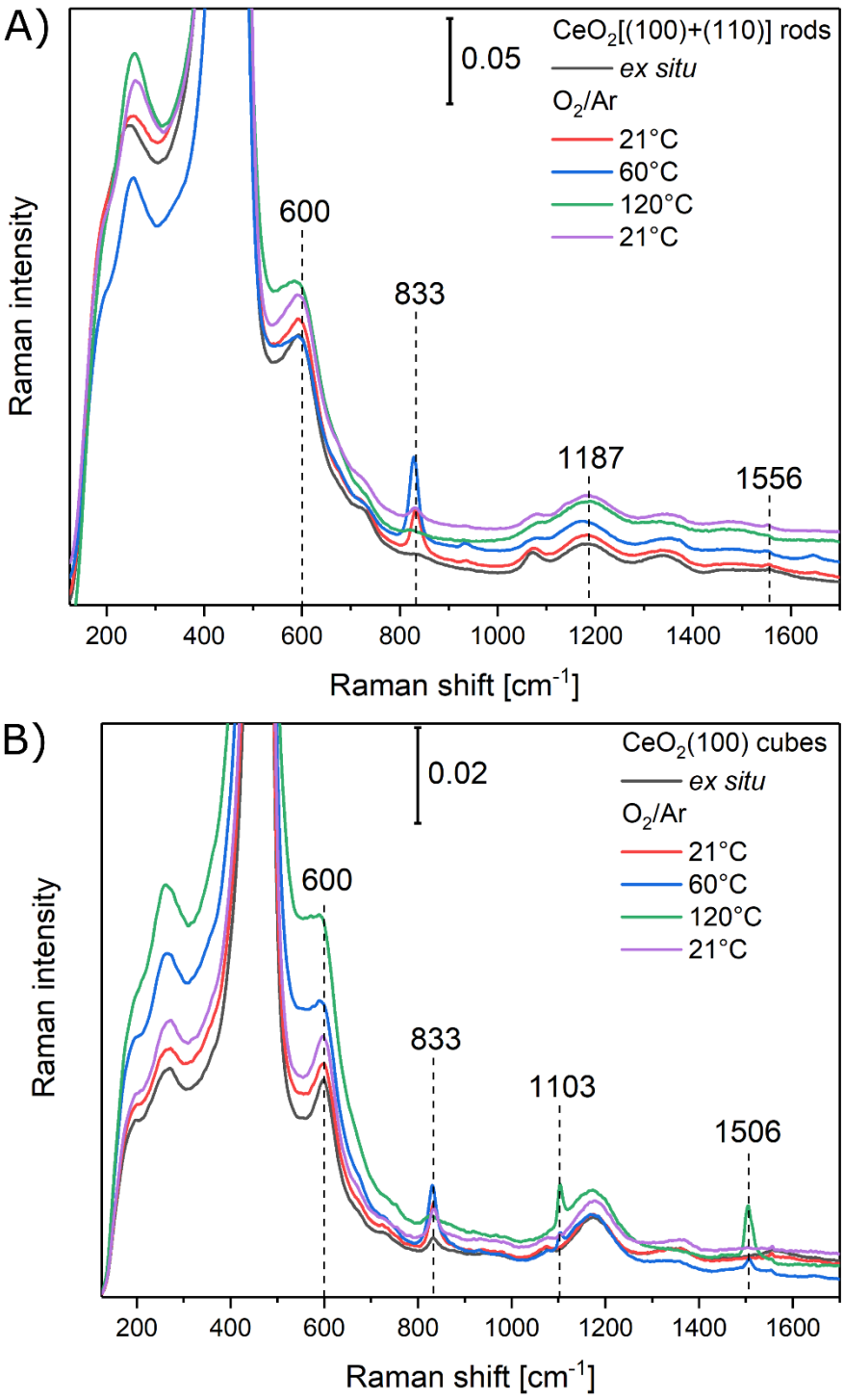

Figure S1: E*x situ* and *in situ* 532 nm Raman spectra of **A)** ceria nanorods and **B)** ceria nanocubes. *In situ* spectra were recorded in 25 % O_2/Ar at the temperatures indicated (total flow rate: 100 mL/min). The high intensity F_{2g} peak at 455 cm^{-1} was cut off to allow an enlarged view of the other features.

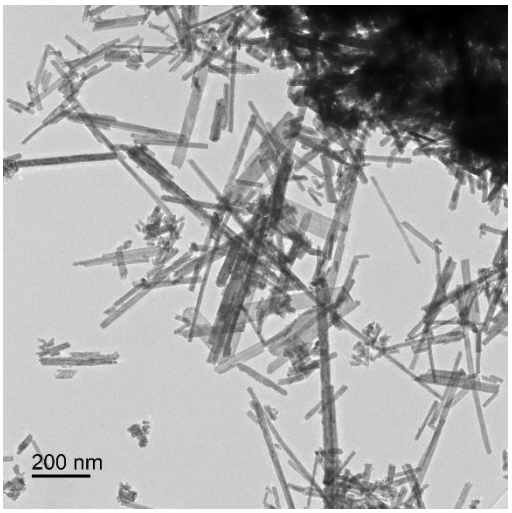

Figure S2: TEM image of ceria nanorods.

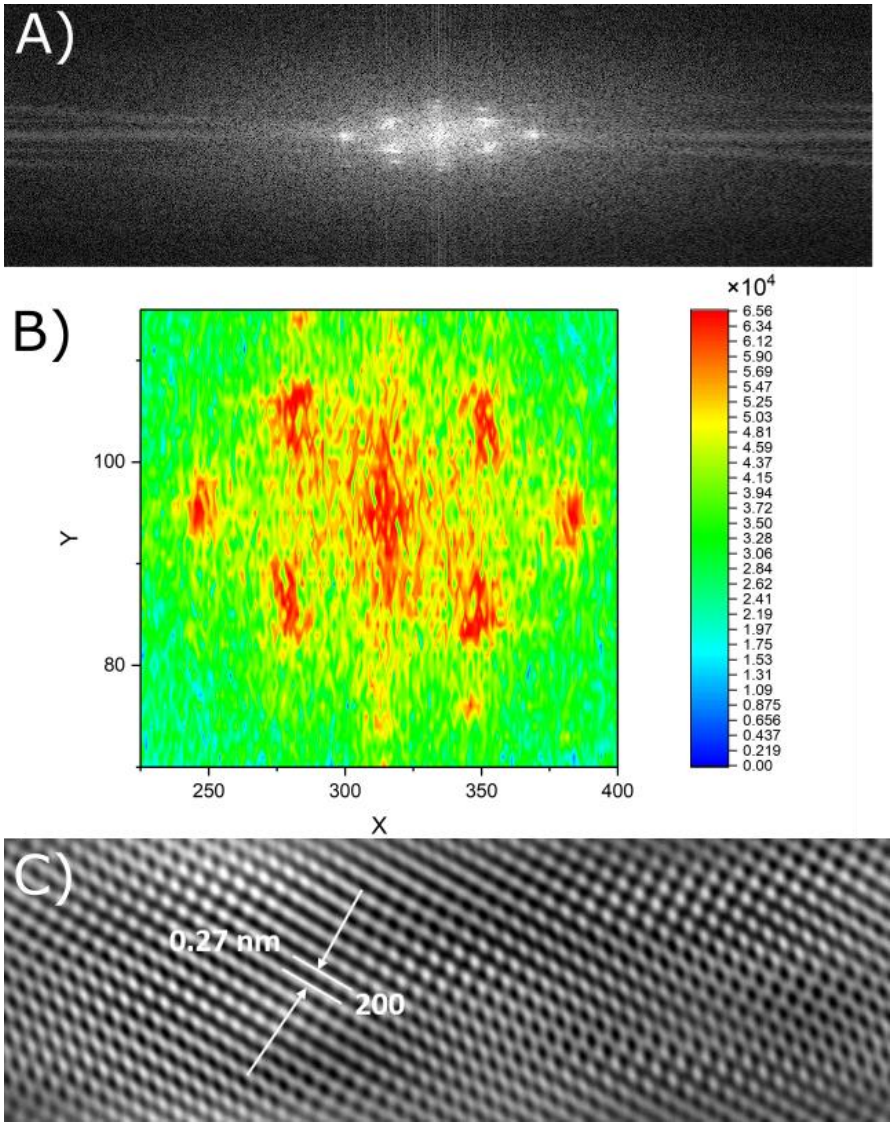

Figure S3: A) FFT diffraction pattern of the CeO_2(100) area in Figure 1A. **B)** Height profile of A). **C)** Inverse FFT of the masked FFT from A). White arrows indicate the 200-lattice plane distance.

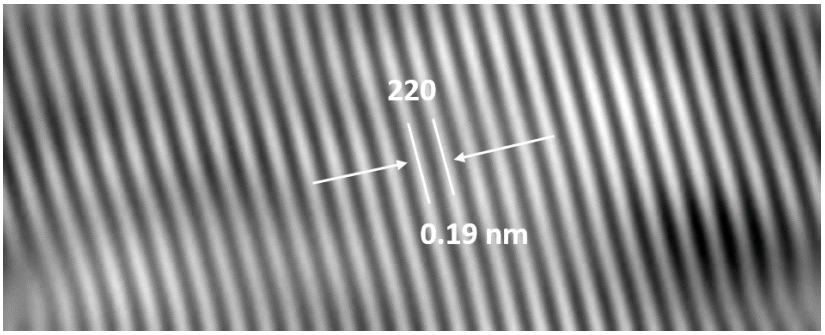

Figure S4: Inverse FFT of a masked diffraction pattern of the CeO_2(110) area. White arrows indicate the 220-lattice plane distance.

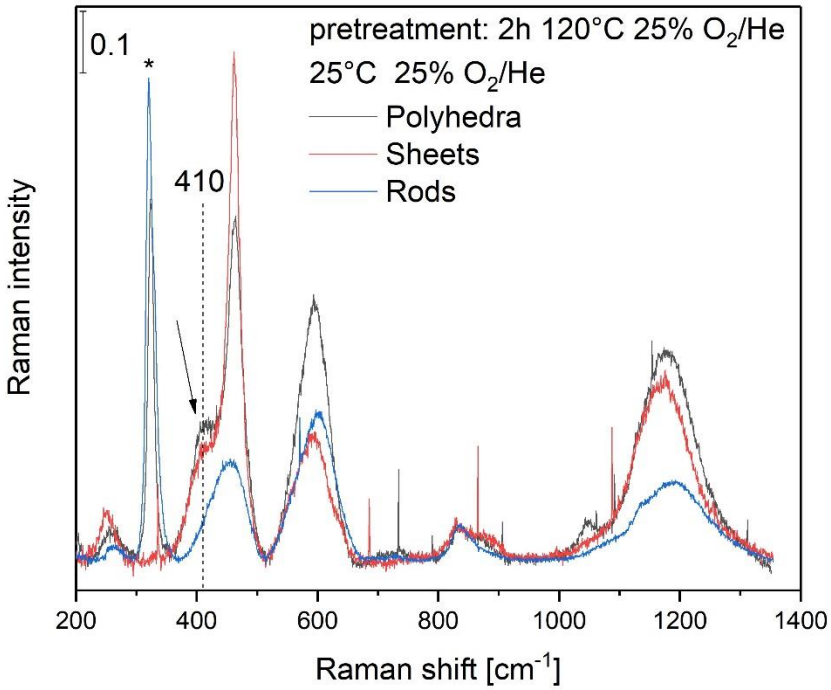

Figure S5: *In situ* 385 nm Raman spectra of ceria sheets, polyhedral, and rods recorded at 25 °C in 25 % O_2/He (pretreatment: 2 h, 120 °C, 25 % O_2/He, 50 mL/min) and at a total flow rate of 50 mL/min. The asterisk (*) marks bands originating from the CaF_2 window, while other sharp features result from cosmic rays. Ceria sheets were measured with a sapphire window, whereby the window features are hidden by the CeO_2 itself, owing to the good focus obtained for the ceria sheets. The band at 410 cm^{-1} results from the longitudinal surface phonon of the CeO_2(111) surface.

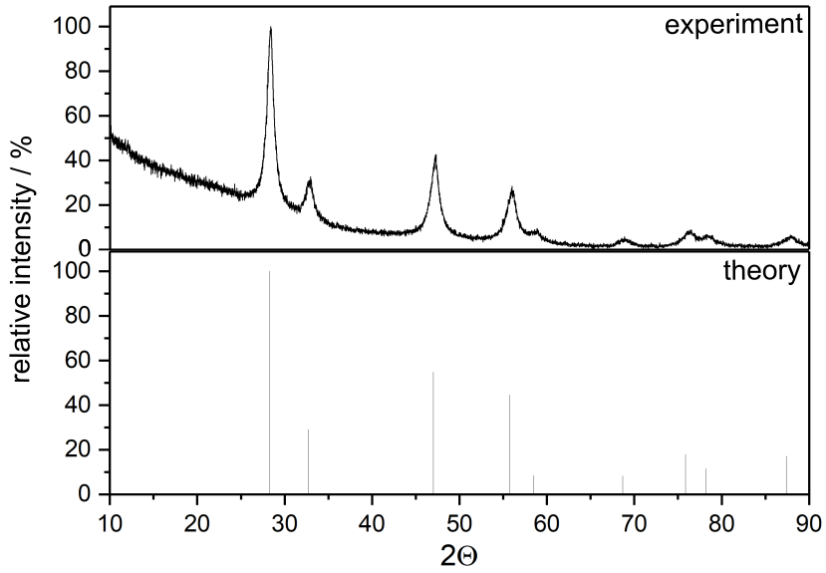

Figure S6: XRD pattern of CeO_2 nanorods (top) in comparison to the pattern of cubic CeO_2 (bottom).

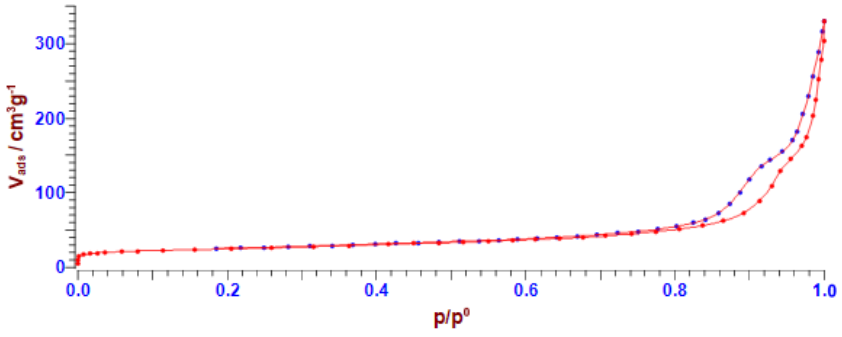

Figure S7: Nitrogen adsorption-desorption isotherm of ceria nanorods.

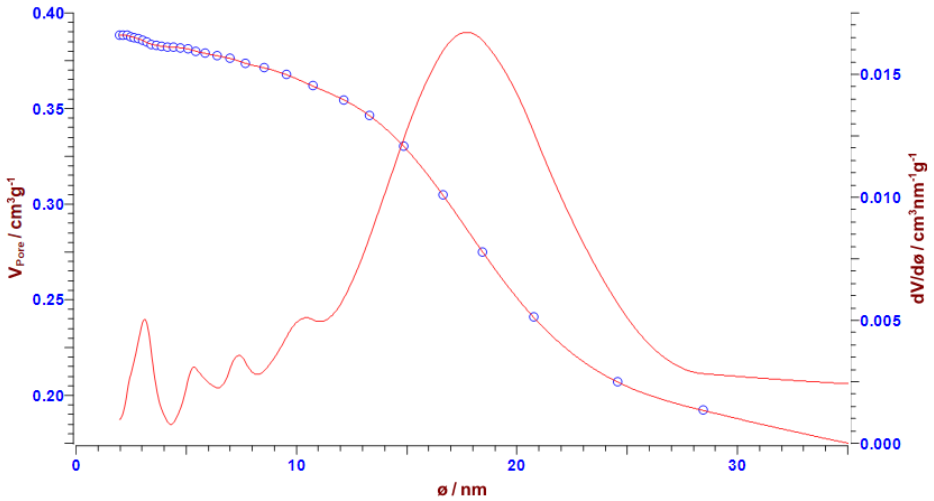

Figure S8: Pore size distribution of ceria nanorods according to the BJH method.

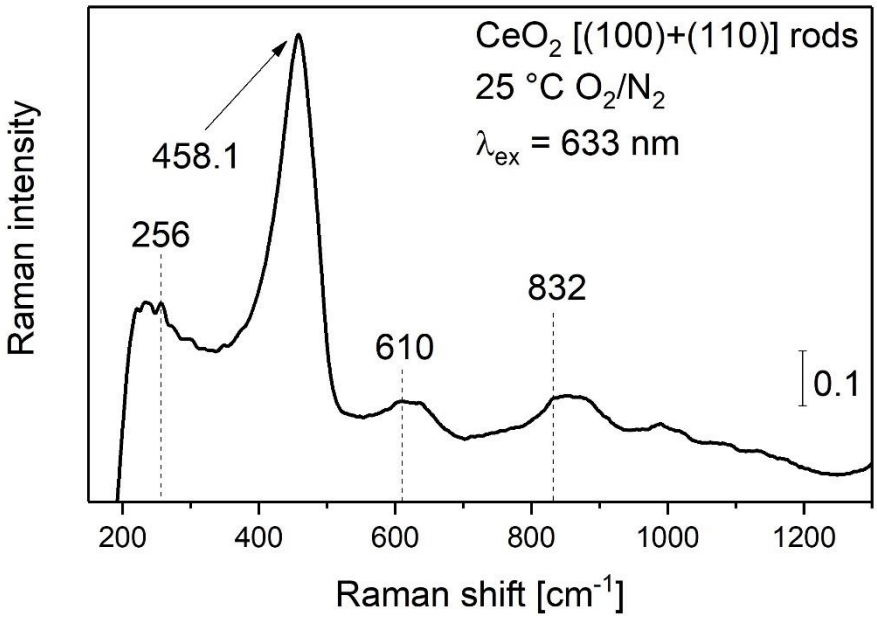

Figure S9: *In situ* 633 nm Raman spectrum of ceria nanorods recorded at 25 °C in 25 % O_2/N_2 (pretreatment: 2 h, 120 °C, 25 % O_2/N_2, 50 mL/min), at a total flow rate of 50 mL/min.

Computational Section

Density Functional Theory Calculations. Calculations were performed using the spin-polarized DFT+U approach as implemented in the Vienna Ab initio Simulation Package (VASP, Version 5.3.5, https://www.vasp.at/), with the generalized gradient approximation of Perdew, Burke and Ernzerhof (PBE)[8] and an U_{eff} parameter of 4.5 eV for the Ce 4f states (PBE+U/4.5 eV). The Ce (4f, 5s, 5p, 5d, 6s) and O (2 s, 2p) electrons were explicitly treated as valence states within the projector augmented wave (PAW) method[9] with a plane-wave cutoff of 400 eV, whereas the remaining electrons were treated as part of the atomic cores. The CeO_2(110) surface was modelled by supercells with (1 × 1), (2 × 1), (2 × 2), and (3 × 3) periodicities with the calculated ceria bulk equilibrium lattice constant (5.484 Å[10]). A slab of seven atomic layers, separated by at least a 10 Å-thick vacuum layer, was used. The slab thickness has been chosen based on the convergence of the calculated surface energy. The sampling of the Brillouin zone is realized by (6 × 4 × 1), (3 × 4 × 1), (3 × 2 × 1) or (1 × 1 × 1) Monkhorst-Pack grids.[11] All atoms in the bottom atomic layer were fixed at their optimized bulk-truncated positions during geometry optimization, whereas the rest of the atoms were allowed to fully relax. Total energies and forces were calculated with a precision of 10^{-6} eV and 10^{-2} eV/Å for electronic and force convergence, respectively.

Reduced extended CeO_{2-x}(110) surfaces were modelled with different concentrations of oxygen vacancies ($\Theta_{O_{vac}}$ = 0.056, 0.125, 0.25, 0.5), see Fig. S10. The positions of the two Ce^{3+} ($4f^1$) polarons,

resulting from the localization of the excess charge left in the system upon the removal of an O atom, were optimized. The oxidation state of a given Ce ion (Ce^{4+} or Ce^{3+}) was determined by considering its local magnetic moment (the difference between up and down spins on the ion), which can be estimated by integrating the site- and angular momentum-projected spin-resolved density of states over spheres with radii chosen as the Wigner−Seitz radii of the PAW potentials. The magnetic moments of the Ce^{4+} ($4f^0$) and Ce^{3+} ($4f^1$) ions are 0 and ∼1 μB, respectively, because the occupations of the Ce 4f states are 0 and ∼1, respectively.

The adsorption of peroxide species on the CeO_{2-x}(110) surfaces were also considered. The O_2^{2-}/CeO_{2-x}(110) structures with varying concentration of oxygen vacancies, $\Theta_{O_{vac}}$, and peroxide species, $\Theta_{O_2^{2-}}$, were optimized (Fig. S11). After relaxation, a normal mode analysis was performed followed by a calculation of the Raman intensities using density functional perturbation theory (DFPT). For more detailed information, and the results for the CeO_2(100) surface, please refer to our previous studies.[7,10]

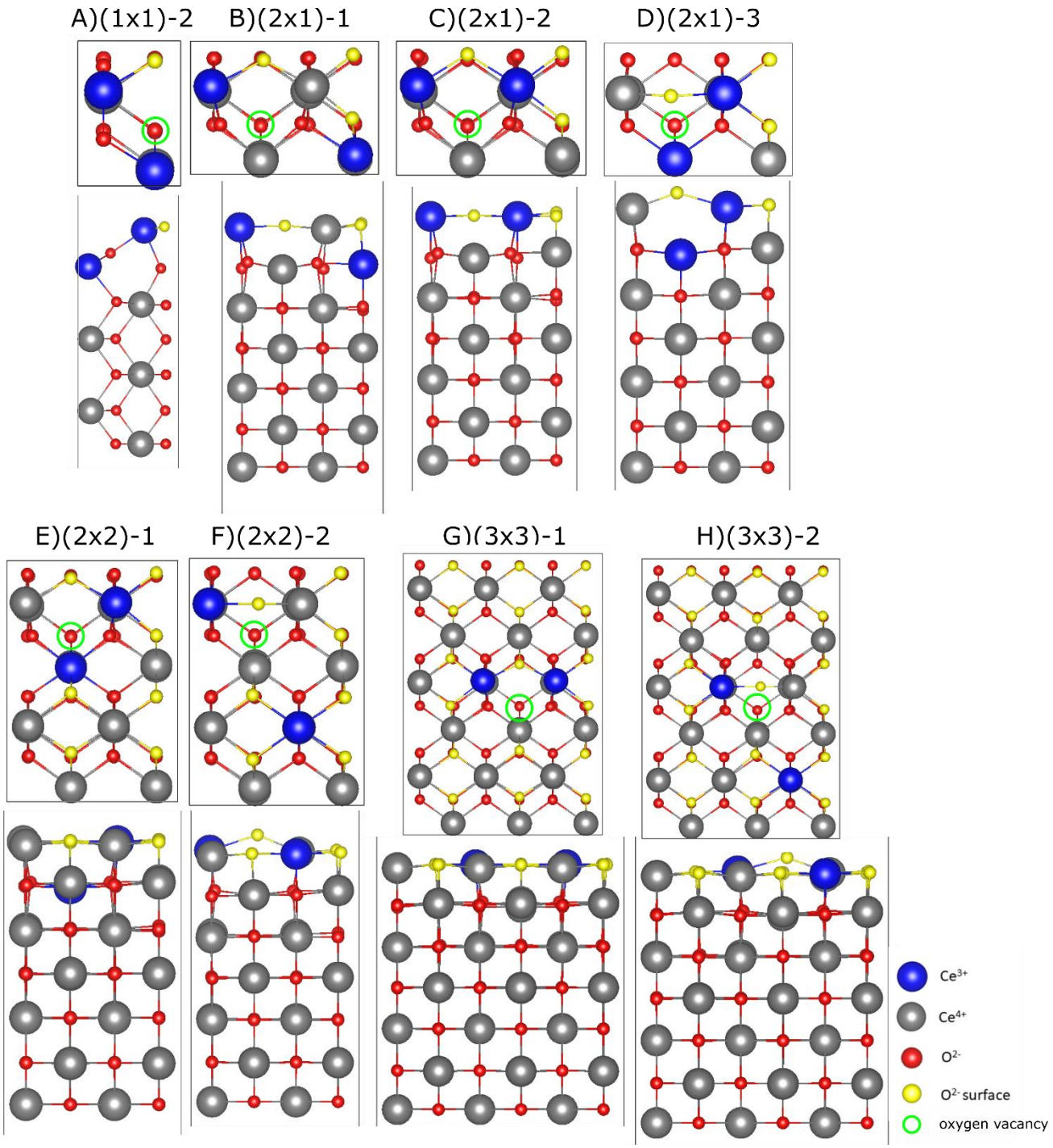

Figure S10: Top and side views of the reduced CeO_{2-x}(110) surface with varying oxygen vacancy concentration. **A)** $\Theta_{O_{vac}}$= 0.5 with (1×1) periodicity **B)** to **D)** $\Theta_{O_{vac}}$= 0.25 with (2×1) periodicity, **E)** and **F)** $\Theta_{O_{vac}}$= 0.125 with (2×2) periodicity, and **G)** and **H)** $\Theta_{O_{vac}}$= 0.056 with (3×3) periodicity. Atoms correspond to Ce^{3+} (blue), Ce^{4+} (grey), O^{2-}(red), surface O^{2-} (yellow), O_2^{2-} (dark blue) and the position of the oxygen vacancy is marked by a green circle.

Table S1: Total energies, E_{tot}, for CeO_{2-x}(110) structures with varying surface oxygen vacancy concentration, $\Theta_{O_{vac}}$. The average oxygen vacancy formation energy, $E_{vac,O}$, is given with respect to ½ O_2 and the clean surface ($E_{O_2} = -9.879$ eV and $E_{CeO_2(110)} = -169.590$, -339.180, -678.362, and -1526.304 eV for the (1×1), (2×1), (2×2), and (3×3) surface unit cells, respectively). The last column compares the $E_{vac,O}$ values with those in the literature, calculated with PBE+U/5 eV (408 eV cutoff)[12] or dispersion-corrected PBE+U/4.5 eV (600 eV cutoff)[13,14]. In parenthesis the labelling of the structures in Ref. 11 is indicated to facilitate the comparison

Structure	$\Theta_{O_{vac}}$	E_{tot} [eV]	$E_{vac,O}$* [eV/atom]	$E_{vac,O}$ (Kullgren *et al.*[12])	$E_{vac,O}$ (Yang *et al.*[13,14])
A) (1×1)-2	0.5	−162.540	2.110	–	–
B) (2×1)-1	0.25	−332.182	2.059	–	–
C) (2×1)-2	0.25	−332.272	1.969	2.31 (s-$InPl_{1+2}$)	–
D) (2×1)-3	0.25	−332.288	1.953	2.48 (u-Bri_{1+8})	–
E) (2×2)-1	0.125	−671.535	1.888	–	–
F) (2×2)-2	0.125	−672.100	1.323	1.74 (u-Bri_{1+4})	1.27
G) (3×3)-1	0.056	−1519.785	1.580	1.91 (s-$InPl_{1+2}$)	–
H) (3×3)-2	0.056	−1520.194	1.170	1.54 (u-Bri_{1+4})	–

* $E_{vac,O} = \frac{1}{n}[E_{CeO_{2-x}(110)} + \frac{n}{2} E_{O_2} - E_{CeO_2(110)}]$, *n* is the number of vacancies in the unit cell

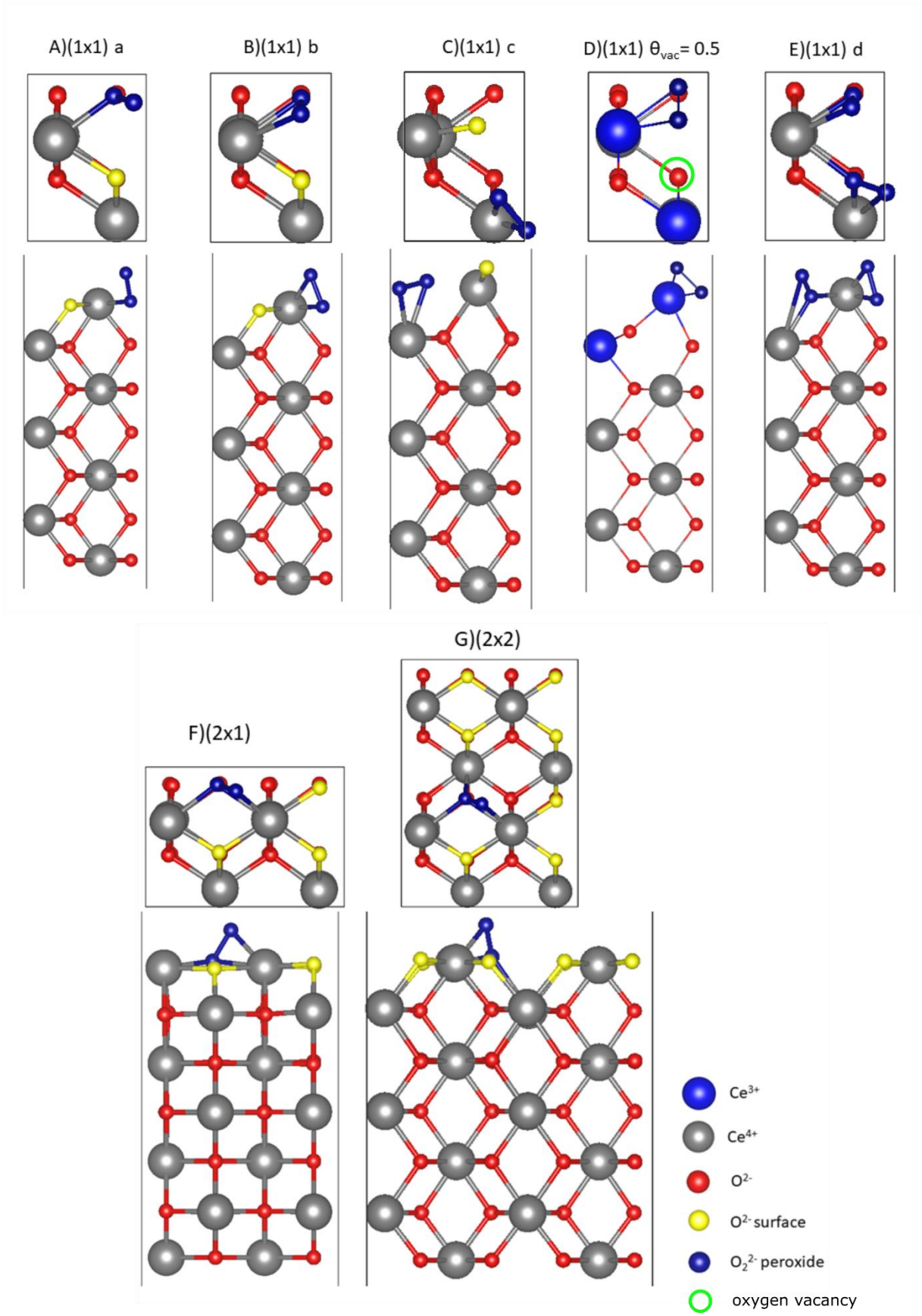

Figure S11: Top and side views of $O_2^{2-}/CeO_{2-x}(110)$ structures with varying concentration of peroxide species. **A)** to **D)** $\Theta_{O_2^{2-}} = 0.5$ and **E)** $\Theta_{O_2^{2-}} = 1$ with (1×1) periodicity. **F)** $\Theta_{O_2^{2-}} = 0.25$ and **G)** $\Theta_{O_2^{2-}} = 0.125$

with (2×1) and (2×2) periodicity, respectively. Atoms correspond to Ce^{3+} (blue), Ce^{4+} (grey), O^{2-}(red), surface O^{2-} (yellow), O_2^{2-} (dark blue), and the position of the oxygen vacancy is marked by a green circle.

Table S2: Total energies, E_{tot}, for peroxide species on the CeO_{2-x}(110) surface with varying concentration $\Theta_{O_2^{2-}}$. For the calculation of the average peroxide adsorption energies, $E_{ads,O_2^{2-}} = -E_{vac,O} + E_{ads,O}$, the average vacancy formation energies, $E_{vac,O}$, from Table S1 were used. For each vacancy concentration, $\Theta_{O_{vac}}$, the most stable defect structure was considered. $E_{ads,O}$ is the average adsorption energy of the O atoms remaining on the healed surface upon O_2^{2-} adsorption (E_{O_2} = –9.879 eV and $E_{CeO_2(110)} = -169.590$, –339.180, and –678.362 eV for the (1×1), (2×1), and (2×2) surface unit cells, respectively). The O–O bond length of the superoxide species and the Raman shifts are also listed.

Structure	$\Theta_{O_{vac}}/\Theta_{O_2^{2-}}$ [ML]	E_{tot} [eV]	$E_{ads,O}$* [eV/atom]	$E_{ads,O_2^{2-}}$# [eV/O_2^{2-}]	O–O bond length [Å]	Raman shift [cm^{-1}]
(1×1) a	0.5/0.5	–174.261	+0.269	–1.842	1.441	920
(1×1) b[a]	0.5/0.5	–174.251	+0.278	–1.832	1.437	948
(1×1) c	0.5/0.5	–173.312	+1.218	–0.829	1.433	919
(1×1) $\Theta_{O_{vac}}$ = 0.5	1/0.5	–167.695	–0.215**	-	1.502	857
(1×1) d	1/1	–178.640	+0.415	-	1.437/1.449	945/915
(2×1)	0.25	–343.962	+0.158	–1.795	1.444	901
(2×2)	0.125	–683.149	+0.153	–1.170	1.445	898

[a]One imaginary frequency (30 cm^{-1}).

*$E_{ads,O} = \frac{1}{m}[E_{O_2^{2-}/CeO_{2-x}(110)} - \frac{m}{2} E_{O_2} - E_{CeO_2(110)}]$, m is the no. of O_2^{2-} species in the unit cell

#$E_{ads,O_2^{2-}} = -E_{vac,O} + E_{ads,O}$

**$E_{ads,O} = E_{O_2^{2-}/CeO_{2-x}(110)} - \frac{1}{2} E_{O_2} - E_{CeO_{2-x}(110)}$ ($\Theta_{O_{vac}} = 0.5$)

Comparison of the $O_2^{2-}/CeO_{2-x}(110)$ and $O_2^{2-}/CeO_{2-x}(100)$ structures with those in previous studies:

Here we compare our results for the $O_2^{2-}/CeO_{2-x}(110)$ and $O_2^{2-}/CeO_{2-x}(100)$ structures with a peroxide concentration of $\Theta_{O_2^{2-}} = 0.125$ ML and (2×2) and *c*(2×2) periodicity, respectively, with those of previous PBE+U studies.[13,15,16] Nolan[15] employed a U_{eff} value of 5 eV (PBE+U/5 eV) to investigate the healing of oxygen vacancies on the reduced $CeO_{2-x}(110)$ and (100) surfaces by peroxide species, modelled by (2×2) and *p*(4×2) surface unit cells, respectively ($\Theta_{O_2^{2-}} = 0.125$ ML). He found that the O–O bond length for peroxide species on $CeO_2(110)$ is 1.44 Å and on $CeO_2(100)$ is 1.42 Å. However, for the same peroxide concentration ($\Theta_{O_2^{2-}} = 0.125$ ML), but not the same species distribution [cf. *p*(4×2)[13] and *c*(2×2) in this work], we found that the O–O bond length of the chemisorbed O_2^{2-} species on the $CeO_2(110)$ facet is smaller by 2.3 pm than on the $CeO_2(100)$ [(2×2)-$CeO_2(110)$: 1.445 Å and *c*(2×2)-$CeO_2(100)$[7]: 1.468 Å], which is in line with a recent dispersion-corrected PBE+U/4.5 eV study by Yang *et al.*[13,14] [(2×2)-$CeO_2(110)$: 1.44 Å and on *p*(2×2)-$CeO_2(100)$: 1.47 Å, $\Theta_{O_2^{2-}} = 0.125$ and 0.25 ML, respectively). Moreover, in our $O_2^{2-}/CeO_{2-x}(100)$ structure, the peroxide species are lying more flat on the surface, as compared to those of Nolan,[15] but in agreement with Yang *et al.*[13] Regarding the adsorption energy of the peroxide species, $E_{ads,\,O_2^{2-}}$, we found that O_2^{2-} species are by 0.56 eV more stable on the $CeO_2(100)$ facet than on the (110) {*c*(2×2)-$CeO_2(100)$[7]: –1.732 eV [*p*(2×2): –2.141] and (2×2)-$CeO_2(110)$: –1.170 eV, Table S2}. Yang *et al.*[13] also found a higher stability of O_2^{2-} species on the $CeO_2(100)$ facet [*p*(2×2)-$CeO_2(100)$: –2.26 eV and on (2×2)-$CeO_2(110)$: –1.23 eV). However, Nolan[15] found comparable adsorption energies [*p*(4×2)-$CeO_2(100)$: –2.02 eV and (2×2)-$CeO_2(110)$: –2.05 eV]. Note that the peroxide adsorption energy is calculated with respect to O_2(gas) and the reduce surface, and that in Ref. 13, the structure employed is likely not to have corresponded to the most stable one with respect to the localization of the excess charge.

In the work of Kullgren *at al.*[16] (PBE+U/5 eV), the formation of intrinsic peroxide species on the (oxidized) $CeO_2(110)$ surface was considered by placing two neighboring surface oxygen atoms close together at typical molecular distances before relaxation with (3×2) periodicity ($\Theta_{O_2^{2-}} = 0.083$ ML). This results in O_2^{2-} species on the surface with O–O bond length of 1.52 Å, where at the same time an oxygen vacancy is present. The calculated energy for intrinsic O_2^{2-} species is 1.35 eV. Please note that here the peroxide formation energies are not comparable with the values in this work, because Kullgren *et al.*[16] assume an oxygen defect free structure as initial state ($E_{ads,\,O_2^{2-}} = E_{O_2^{2-}/CeO_{2-x}(110)} - E_{CeO_2(110)}$), which in turn explains the endothermic formation energy. We have considered a similar type of structure (D in Fig. S11) at a higher peroxide concentration ($\Theta_{O_2^{2-}} = 0.5$ ML), for which the O–O bond length is 1.50 Å. If we would calculate $E_{ads,\,O_2^{2-}}$ as in the work of Kullgren *at al.*[16], our value would be 1.9 eV.

Table S3: Comparison of literature values for $E_{ads,O_2^{2-}}$ and O–O bond lengths for the most stable O_2^{2-} species on the CeO_2(110) facet with a concentration of $\Theta_{O_2^{2-}} = 0.125$ and on the CeO_2(100) facet with a concentration of $\Theta_{O_2^{2-}} = 0.125$ and 0.25. The reference is given in the last column.

Structure	$\Theta_{O_2^{2-}}$ [ML]	$E_{ads,O_2^{2-}}$ [eV/O_2^{2-}]	O–O bond length [Å]	Ref.
		CeO_2(110)		
(2×2)	0.125	–1.17	1.45	This work
(2×2)	0.125	–2.05	1.44	Nolan[15]
(2×2)	0.125	–1.23	1.44	Yang *et al.*[13,14]
		CeO_2(100)		
c(2×2)	0.125	–1.73	1.47	Schilling *et al.*[7]
p(2×2)	0.25	–2.14	1.47	Schilling *et al.*[7]
p(2×4)	0.125	–2.02	1.42	Nolan[15]
p(2×2)	0.25	–2.26	1.47	Yang *et al.*[13]

References

(1) Wu, Q.; Zhang, F.; Xiao, P.; Tao, H.; Wang, X.; Hu, Z.; Lü, Y. Great Influence of Anions for Controllable Synthesis of CeO_2 Nanostructures: From Nanorods to Nanocubes. *J. Phys. Chem. C* **2008**, *112* (44), 17076–17080.

(2) Mai, H.-X.; Sun, L.-D.; Zhang, Y.-W.; Si, R.; Feng, W.; Zhang, H.-P.; Liu, H.-C.; Yan, C.-H. Shape-Selective Synthesis and Oxygen Storage Behavior of Ceria Nanopolyhedra, Nanorods, and Nanocubes. *J. Phys. Chem. B* **2005**, *109* (51), 24380–24385.

(3) Brunauer, S.; Emmett, P. H.; Teller, E. Adsorption of Gases in Multimolecular Layers. *J. Am. Chem. Soc.* **1938**, *60* (2), 309–319.

(4) Nitsche, D.; Hess, C. In Situ Diagnostics of Catalytic Materials Using Tunable Confocal Raman Spectroscopy. *J. Raman Spectrosc.* **2013**, *44* (12), 1733–1738.

(5) Waleska, P. S.; Hess, C. Oligomerization of Supported Vanadia: Structural Insight Using Surface-Science Models with Chemical Complexity. *J. Phys. Chem. C* **2016**, *120* (33), 18510–18519.

(6) Schilling, C.; Hess, C. CO Oxidation on Ceria Supported Gold Catalysts Studied by Combined Operando Raman/UV–Vis and IR Spectroscopy. *Top. Catal.* **2017**, *60* (1–2), 131–140.

(7) Schilling, C.; Ganduglia-Pirovano, M. V.; Hess, C. Experimental and Theoretical Study on the Nature of Adsorbed Oxygen Species on Shaped Ceria Nanoparticles. *J. Phys. Chem. Lett.* **2018**, *9* (22), 6593–6598.

(8) Perdew, J. P.; Burke, K.; Ernzerhof, M. Generalized Gradient Approximation Made Simple. *Phys. Rev. Lett.* **1996**, *77* (18), 3865–3868.

(9) Blöchl, P. E. Projector Augmented-Wave Method. *Phys. Rev. B* **1994**, *50* (24), 17953–17979.

(10) Schilling, C.; Hofmann, A.; Hess, C.; Ganduglia-Pirovano, M. V. Raman Spectra of Polycrystalline CeO_2: A Density Functional Theory Study. *J. Phys. Chem. C* **2017**, *121* (38), 20834–20849.

(11) Monkhorst, H. J.; Pack, J. D. Special Points for Brillouin-Zone Integrations. *Phys. Rev. B* **1976**, *13* (12), 5188–5192.

(12) Kullgren, J.; Hermansson, K.; Castleton, C. Many Competing Ceria (110) Oxygen Vacancy Structures: From Small to Large Supercells. *J. Chem. Phys.* **2012**, *137* (4), 044705.

(13) Yang, C.; Yu, X.; Heißler, S.; Weidler, P. G.; Nefedov, A.; Wang, Y.; Wöll, C.; Kropp, T.; Paier, J.; Sauer, J. O_2 Activation on Ceria Catalysts-The Importance of Substrate Crystallographic Orientation. *Angew. Chem. Int. Ed.* **2017**, *56* (51), 16399–16404.

(14) The PBE+D2 defect formation energy of 1.27 eV (122 kJ/mol) was obtained in a personal communication (T. Kropp, 3.04.2020).

(15) Nolan, M. Healing of Oxygen Vacancies on Reduced Surfaces of Gold-Doped Ceria. *J. Chem. Phys.* **2009**, *130* (14), 144702.

(16) Kullgren, J.; Hermansson, K.; Broqvist, P. Reactive Oxygen Species in Stoichiometric Ceria: Bulk and Low-Index Surfaces. *Phys. Status Solidi RRL* **2014**, *8* (6), 600–604.